Research in Astronomy and Astrophysics, 25:035007 (10pp), 2025 March

https://doi.org/10.1088/1674-4527/adb36c
CSTR: 32081.14.RAA.adb36c

TSC: Efficient FRB Signal Search by a Two-stage Cascade Deep Learning Model on FAST

Ronghuan Yan[1,2], Junlin Li[1,2], Weixin Tian[1,2], and Nyasha Mkwanda[1,2]
[1] Hubei Key Laboratory of Intelligent Vision Based Monitoring for Hydroelectric Engineering, China Three Gorges University, Yichang 443002, China; t_wxin@126.com
[2] College of Computer and Information Technology, China Three Gorges University, Yichang 443002, China
Received 2024 June 10; revised 2025 January 9; accepted 2025 January 22; published 2025 March 10

Abstract

Fast Radio Bursts (FRBs) have emerged as one of the most intriguing and enigmatic phenomena in the field of radio astronomy. The key of current related research is to obtain enough FRB signals. Computer-aided search is necessary for that task. Considering the scarcity of FRB signals and massive observation data, the main challenge is about searching speed, accuracy and recall. in this paper, we propose a new FRB search method based on Commensal Radio Astronomy FAST Survey (CRAFTS) data. The CRAFTS drift survey data provide extensive sky coverage and high sensitivity, which significantly enhance the probability of detecting transient signals like FRBs. The search process is separated into two stages on the knowledge of the FRB signal with the structural isomorphism, while a different deep learning model is adopted in each stage. To evaluate the proposed method, FRB signal data sets based on FAST observation data are developed combining simulation FRB signals and real FRB signals. Compared with the benchmark method, the proposed method F-score achieved 0.951, and the associated recall achieved 0.936. The method has been applied to search for FRB signals in raw FAST data. The code and data sets used in the paper are available at github.com/aoxipo.

Key words: techniques: image processing – techniques: high angular resolution – techniques: interferometric

1. Introduction

Since the first Fast Radio Burst (FRB) signal was discovered in 2007 (Lorimer et al. 2007), FRBs have garnered significant attention in the field of astronomy. Many institutes such as the Green Bank Telescope (Prestage et al. 2009), Parkes Observatory Telescope (Hobbs et al. 2011), the UTMOST project (Bailes et al. 2017) and the Square Kilometre Array (Dewdney et al. 2009) have conducted extensive observational research on FRBs. The Five-hundred-meter Aperture Spherical radio Telescope (FAST; Li et al. 2018), developed by China independently, with high-precision detection capability and sensitivity, incorporates unique advantages for FRB detection.

The traditional machine learning search method mainly adopts the method based on de-dispersion (Thompson et al. 2011; Wagstaff et al. 2016; Foster et al. 2017; Farah et al. 2018, 2019; Li et al. 2018; Michilli et al. 2018; Madison et al. 2019; Yatawatta et al. 2019; Gupta et al. 2021; Morello et al. 2021). The method employs various machine learning algorithms (such as support vector machines, random forests, etc.) for training and testing to compare the performance of different models which exhibits notable advantages, including high accuracy and effective signal recovery capabilities, rendering it suitable for high-precision research on FRBs. Nevertheless, it is also associated with certain drawbacks, particularly regarding computational cost and processing speed.

In contrast, deep learning-based approaches have great advantages in speed and have been widely adopted in recent years. Those approaches can be divided into two sub-categories according to de-dispersion or not.

Regarding methods based on de-dispersion, Connor & Van Leeuwen (2018) used several types of input data, including the dispersive dynamic spectrum, dispersion measure(DM)–time array, time series, and multibeam detection signal-to-noise information. These inputs were processed separately using a two-dimensional Convolutional Neural Network (2D CNN), a one-dimensional Convolutional Neural Network (1D CNN), and a forward Neural Network (FNN), to extract features. The extracted features were then integrated into the fully connected layer to classify candidates. Using this approach, they achieved a recall of 99.7% and an accuracy of 99% for single-pulse identification of pulsars. Devansh et al. (2020) provided 11 different models to construct a classification network using frequency and dispersion-time information to identify FRB signals in candidates based on eight different deep learning models and their best method achieved and accuracy of 99.88%, recall of 99.92%, and F-score of 99.87% on the relevant data set. However, the actual FRB samples are utilized less frequently; therefore, despite its exceptional performance on the test set, the model's efficacy may diminish when applied to entirely novel data. Furthermore, the input data require de-dispersion, which significantly reduces the model's processing speed. The common

characteristic of these technologies lies in the application of deep learning to the search and detection of dispersed candidate objects, demonstrating a high degree of reliability.

However, the disadvantage of this method is that it is still accompanied by the time cost of de-dispersion operation in the overall search process (It is evident from Table 8 that there exists a limitation in its speed).

In this context, Zhang proposed that the saliency map can improve the model accuracy by enhancing the brightness variation in images of transient features, by constructing a simple Deep Neural Network (DNN) model and influencing the predicted probability scores by pixel order low-mass pulse signaling so as to perform gradient integration for a given pixel and capturing the luminance variation of smooth pixels in the pulse and thus identifying the FRB signal against complex background noise (Zhang et al. 2020). The complicated de-dispersion step can be avoided by using a deep learning algorithm to search for FRB signals directly on the raw signal. Zhang et al. proposed a ResNet structure consisting of 17 convolutional layers trained on the raw signal without de-dispersion to identify FRB signals, and achieved recall of 88% and precision of 98% (Zhang et al. 2018). Liu et al. proposed a decentralized dynamic spectral search (DDSS) pipeline that searches for FRB signals directly on the raw data, using ResNetV2 and Xception Net models as the feature extraction part of their processing flow. The accuracy of its algorithm reached more than 99.6% (Liu et al. 2022), but the targeted data set dispersion range is only from 100 to 500 pc cm^{-3}.

Despite progress, this method still faces challenges like radio frequency interference (RFI) (Wu et al. 2021), sensitivity to training data distribution, and difficulties with high-resolution backgrounds. Prior research focused on model architectures and lightweight networks to improve search efficiency, but overlooked the inherent isomorphism of FRB signals. This isomorphism means that a portion of an FRB signal is structurally and characteristically similar to the whole signal. While learning FRB features enhances accuracy, it lacks flexibility to capture intricate details.

To enhance the efficiency and accuracy of FRB signal search, we present a two-stage cascade deep learning method that intuitively aligns with the search process. By leveraging the high time resolution and frequency resolution of the drift survey data, our method efficiently identifies FRB signals while addressing challenges such as RFI and baseline drift. Unlike traditional approaches, our method does not rely on the de-dispersion method and directly operates on raw data. By sequentially learning the signal's intensity distribution and dispersion structure features, our approach exhibits remarkable flexibility and performance. In the first stage, we employ the Efficient-Net model to detect the shape and intensity features of FRB signals. Subsequently, in the second stage, we utilize a global attention (GA) model to identify the positional features of FRB signals. By first performing an initial detection and then refining it in the second stage, we aim to achieve efficient and accurate detection of FRB signals. The main contributions of the paper are:

1. Three data sets by combining simulation FRB signals and real FRB signals were developed.
2. A two-stage cascade deep learning model-based search method was proposed with advantages in search speed, accuracy, and recall rate.

2. Datasets

To research a deep learning model-based FRB search algorithm, we developed three image data sets (Dataset-I, Dataset-II, Dataset-III) mainly on simulation FRB signals and partly on real FRB signals, annotated by a computer-aided approach.

2.1. FRB Signal Simulation

The FAST-mode simulation FRB signal can be obtained by superimposing the simulation FRB signal on the background of the FAST observation data. The consistency between the simulation FRB signals and the real FRB signals is of significant impact on the data set. The simulation FRB signals are generated according the method proposed by Niu et al. (2021), taking into account the parameters such as DM, peak signal-to-noise ratio, pulse width and so on. The dispersion estimation equation is defined as

$$\mathrm{DM}_{\mathrm{obs}} = \mathrm{Max}\left\{\sum\left(\frac{d_I(\mathrm{DM},\ t)}{d_t}\right)^2\right\}. \tag{1}$$

Here I (DM, t) represents the equation of a plane wave at a given DM and sampling time t. The dispersion degree of each point in the duration of the simulated signal is constructed by estimating the maximum dispersion.

Using the simulated brightness of the FRB within the beam size and the beam response, we calculate the received peak flux density to simulating the intensity distribution of the FRB signal

$$\phi(l)d_l = \phi^*\left(\frac{l}{l^*}\right)^{\alpha} e^{-\frac{l}{l^*}} d\left(\frac{l}{l^*}\right)\mathrm{SN}. \tag{2}$$

Here α represents the power-law fluid. l^* is luminosity, l is intrinsic luminosity of FRB, and SN is peak signal-to-noise ratio.

The pulse width can be defined as

$$f_{\mathrm{pw}(x)} = \left(\frac{1}{x^2} - \frac{1}{f_s^2}\right), \tag{3}$$

where $x \in (f_s, f_e)$, f_s represents initial frequency, f_e represents termination frequency, and T_{samp} represents the unit sampling time.

Table 1
Parameter Distribution for Simulated FRBs

Parameter	Distribution	Range
DM	Uniform	50, 4550
Pulse Width	Uniform	0.25, 50.25
Fluence (MHz)	Uniform	1125∼1375
Signal Strength	Uniform	1,10
Scattering Timescale	Uniform	0, Width

The final simulation generation is expressed below

$$f_{\mathrm{sim}(x)} = \frac{D^{*}DM}{T_{\mathrm{samp}}} {}^{*} f_{\mathrm{pw}(x)} {}^{*} \int \phi(l)\, dl. \tag{4}$$

Here $x \in (f_s, f_e)$, and D represents a constant.

FITS-format FAST observation data from the Commensal Radio Astronomy FAST Survey (CRAFTS) drift survey were chosen as the background for superimposing simulation signals. The CRAFTS drift survey data provide a large field of sky coverage and high sensitivity, which are essential for detecting transient signals like FRBs. To avoid low probability events such as real FRB signals being in the background accidentally, each background file was viewed manually. Generally, each FITS file of FAST observation data with a bandwidth of 500 MHz and 4096 channels can be transformed to an image with shape of 4096 × 22144, for 12.8849 s total observation time and 4.9152e-05 s sampling time. The parameters for simulating an FRB signal are listed in Table 1.

The FITS images, after superimposing the simulated FRB signal on the background, are displayed in Figure 1.

2.2. Collecting the Datasets

After superimposing the simulation FRB signal on the FAST observation data background, Dataset-I with image shape of 4096 × 4096 and Dataset-II with image shape of 512 × 512 were produced by segmenting the image of the FITS-format superimposed data to samples. By recording the superimposed position combined with the from to frequency in simulation, a computer-aided approach was used to label the samples after calculating the segmenting position, duration, sampling time and the image width and height of samples.

For Dataset-I, the image samples were generated by dividing the entire image every 4096 pixels along the time axis.

For Dataset-II, image samples were obtained by further segmentation of image samples in different backgrounds with the same production method as Dataset I. Each image sample in Dataset-I was segmented into eight equal parts in width and height individually, then we had image samples with shape of 512 × 512. Samples in Dataset-I and samples in Dataset-II by partitioning samples from Dataset-I are illustrated in Figures 2 and 3 respectively.

Dataset-III was created using currently discovered real FRB signals on FAST observation data, which were published on the FAST search to public signal platform CSTCloud https://fast.cstcloud.cn/datavolume/10.1038.s41586-021-03878-5 (Li et al. 2021). A total of 60 FITS files were selected. After separating from Dataset-I and labeling manually, a total of 2661 data with sizes of 4096 × 4096 were marked, including 74 positive samples and 2587 negative samples.

The image sizes, simulation parameters and samples of the three data sets are shown in Table 2.

3. Method

3.1. Isomorphism of FRB Signals

The FRB signal exhibits isomorphism in shape. When a small part of the signal is segmented from an FRB signal that is considered complete, it still retains the main characteristics of the FRB signal, such as high energy, dispersion, etc., and only the duration becomes shorter. This feature provides significant advantages for the detection and analysis of FRB signals. Based on this feature, we have developed a two-stage search method that integrates partial recognition with overall recognition.

In the initial stage, local recognition is conducted by segmenting extensive observation data into smaller time windows, and then searching for signal segments with FRB characteristics within these small time windows. This approach efficiently filters potential FRB candidate signals, thereby significantly decreasing the amount of data that requires detailed analysis.

In the second stage, a comprehensive recognition is undertaken to conduct a more detailed analysis of the candidate signals filtered in the initial stage, reconstructing the complete signal to verify its classification as an FRB and performing in-depth feature extraction and classification. This method enhances the search speed through rapid local recognition, enabling the quick elimination of a large amount of irrelevant data. Meanwhile, the overall recognition stage effectively reduces false positives and improves the reliability of FRB identification, as shown in Figure 4.

When a part of an FRB signal is taken from an entire FRB signal, it will still be detected as an FRB signal.

3.2. Model Architecture

Considering the isomorphism of FRB signals, we proposed a cascade model (TSC-Model) with two stages to search for the FRB signal in FAST observation data. TSC-Model mainly consists of two components. One is Model-I, which was trained to detect whether there is an FRB signal in a 512 × 512 shaped image. The other is Model-II, which was trained to detect whether there is an FBR signal in an 8 × 8 shaped 2-bit image. The architecture of TSC-Model is illustrated in Figure 5.

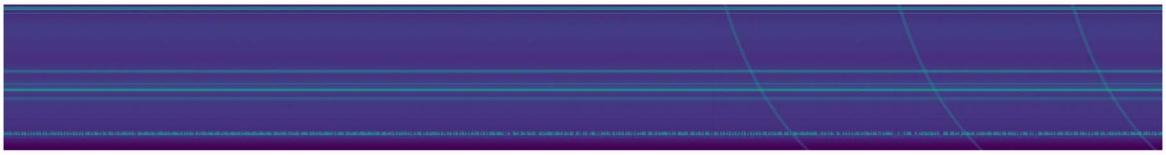

Figure 1. Images of FAST Observation Data After Injection of Simulated FRB Signal (Partial).

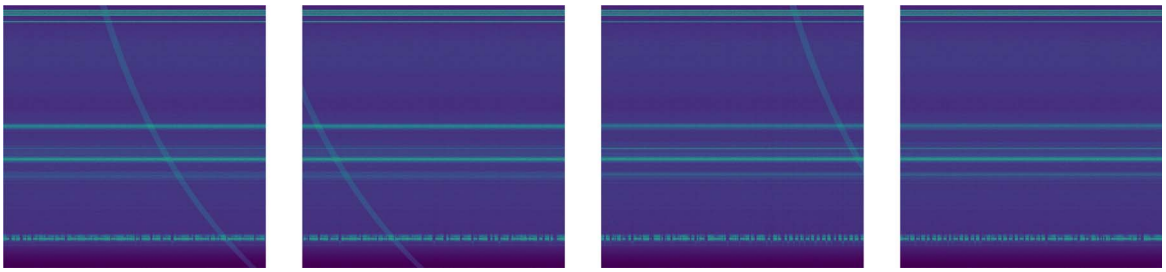

Figure 2. Samples in Dataset-I (4096 × 4096).

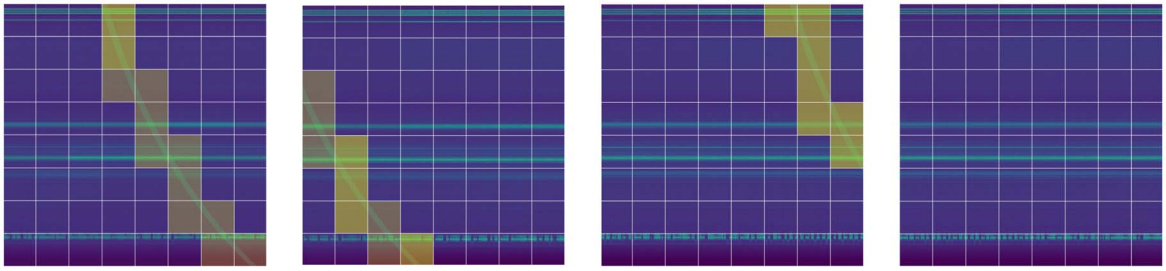

Figure 3. Samples in Dataset-II by partitioning samples from Dataset-I (each sample in Dataset-I is partitioned to 8 × 8 samples in Dataset-II, and yellow blocks are labeled by computer as positive).

When applying the TSC-Model to search for an FRB signal in FAST observation data, the process can be separated into two stages. The process is shown in Figure 6, taking a FITS file as an example.

In the first stage, a FAST observational image in FITS format is used as the input. FITS data typically consist of multidimensional arrays, which we reshape into a two-dimensional array (time × channel) for subsequent analysis. To mitigate baseline drift in the observational data, baseline correction is performed by subtracting the mean value from each channel. Finally, the data are binarized using Otsu's thresholding method. This process enhances the contrast between potential FRB signals and background noise, making subsequent stages of analysis more efficient and accurate. Following the binarization process, the data are divided into blocks of size 4096 × 4096, which are further subdivided into 8 × 8 sub-blocks, each with dimension of 512 × 512 pixels. These 64 sub-images, each sized 512 × 512, are then fed into Model-I to predict the presence of any FRB signals. The prediction results are compiled into a list of length 64, which is subsequently reshaped into an 8 × 8 2-bit image. This image is then used as input for Model-II for further analysis.

In the second stage, each 8 × 8 shaped 2-bit image is fed into Model-II for prediction. If the prediction result is correct, it indicates the presence of an FRB signal within the corresponding 4096 × 4096 image. As long as any of the segmented blocks are predicted to contain an FRB signal, the FAST observational image can be determined to include an FRB signal.

4. Experiment and Result

4.1. Model-I

We choose ResNet, Inception-ResNet (Szegedy et al. 2017), DenseNet (Huang et al. 2011), and Efficient-Net (Tan & Le 2019) as candidate models for Model-I, and Dataset-II was used to train and test. The proportion of the training set, validation set and test set is 40%, 10% and 50% respectively.

Table 2
The Number of Data Set Samples Under various Parameters (PW Stands for Pulse Width, DM for Dispersion Measure, and SN for Peak Signal-to-Noise Ratio, The Third, Fourth, Fifth, Sixth, Seventh and Eighth Columns Respectively Represent the Number of Simulated FRBS in the Range (N, M] of PW, DM, and SN

DataSet	Size	Range (PW)	Num (PW)	Range (DM)	Num (DM)	Range (SN)	Num (SN)	Positive	Negative
Dataset-I	(4096, 4096)	(0.25, 1.25]	448	(0, 50]	548	(0, 1]	548	5711	5711
		(1.25, 5.25]	490	(50, 550]	594	(1, 2]	594	…	…
		(5.25, 10.25]	542	(550, 1050]	558	(2, 3]	558	…	…
		(10.25, 15.25]	521	(1050, 1550]	502	(3, 4]	502	…	…
		(15.25, 20.25]	517	(1550, 2050]	610	(4, 5]	610	…	…
		(20.25, 25.25]	594	(2050, 2550]	534	(5, 6]	534	…	…
		(25.25, 30.25]	382	(2550, 3050]	444	(6, 7]	444	…	…
		(30.25, 35.25]	422	(3050, 3550]	492	(7, 8]	492	…	…
		(35.25, 40.25]	462	(3550, 4050]	500	(8, 9]	500	…	…
		(40.25, 45.25]	462	(4050, 4550]	533	(9, 10]	533	…	…
		(45.25, 55.25]	475	…	…	…	…	…	…
Dataset-II	(512,512)	(0.25, 1.25]	5404	(0, 50]	5831	(0, 1]	5831	48376	541064
		(1.25, 5.25]	5573	(50, 550]	6242	(1, 2]	6242	…	…
		(5.25, 10.25]	4821	(550, 1050]	5114	(2, 3]	5114	…	…
		(10.25, 15.25]	4458	(1050, 1550]	4727	(3, 4]	4727	…	…
		(15.25, 20.25]	4306	(1550, 2050]	5058	(4, 5]	5058	…	…
		(20.25, 25.25]	4955	(2050, 2550]	4431	(5, 6]	4431	…	…
		(25.25, 30.25]	3077	(2550, 3050]	3571	(6, 7]	3571	…	…
		(30.25, 35.25]	3401	(3050, 3550]	3980	(7, 8]	3980	…	…
		(35.25, 40.25]	3728	(3550, 4050]	4221	(8, 9]	4221	…	…
		(40.25, 45.25]	3982	(4050, 4550]	5201	(9, 10]	5201	…	…
		(45.25, 55.25]	4671	…	…	…	…	…	…
Dataset-III	(4096, 4096)	…	…	…	…	…	…	74	2587

Note. The last two columns represent the total number of positive and negative samples.

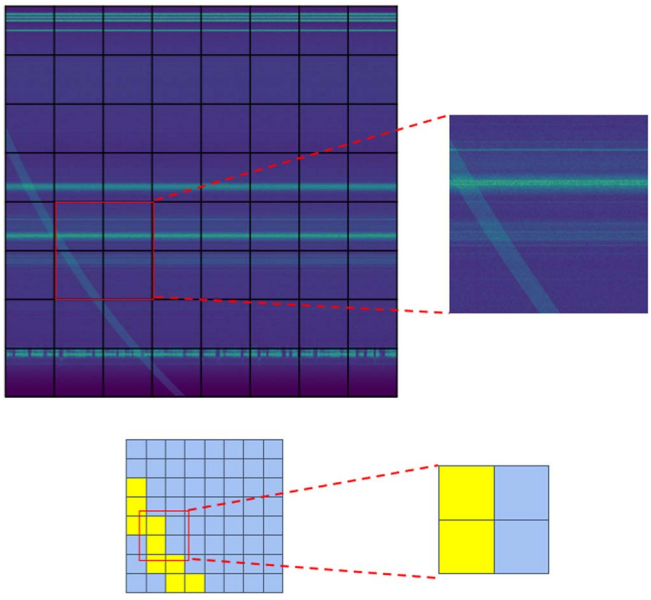

Figure 4. Isomorphism of FRB signals.

We use the Adam optimization algorithm (Kingma & Ba 2014) , and set the learning rate to 0.00001 and the weight decay rate to 0.001, using the cross-entropy loss function as the objective function. To prevent overfitting due to too many training iterations, we use early stopping and set the patience to 5 during training, which means that if the model lasts 5 rounds and does not converge on the validation set, the training is stopped early.

The training process of the four models is shown in Figure 7.

The testing results of the four models are shown in Table 3.

4.2. Model-II

The goal of Model-II is to predict on 8 × 8 shape in 2-bit images, which is a relatively easy task. We employed the GA model (Abujar et al. 2021) to do that.

To train the GA Model, we produced a temporary data set. The positive samples were generated from Dataset-I and Dataset-II, utilizing the correspondence between the two data sets. The negative samples were generated to zero-matrix or random matrix manually. Examples of training samples are shown in Figure 8.

The number of samples in this temporary data set is 11422, with 5711 positive samples and 5711 negative samples. The proportion of the training set, validation set and test set is 40%, 10% and 50% respectively.

The training result for Model-II is shown in Table 4.

The test result for Model-II is shown in Table 5.

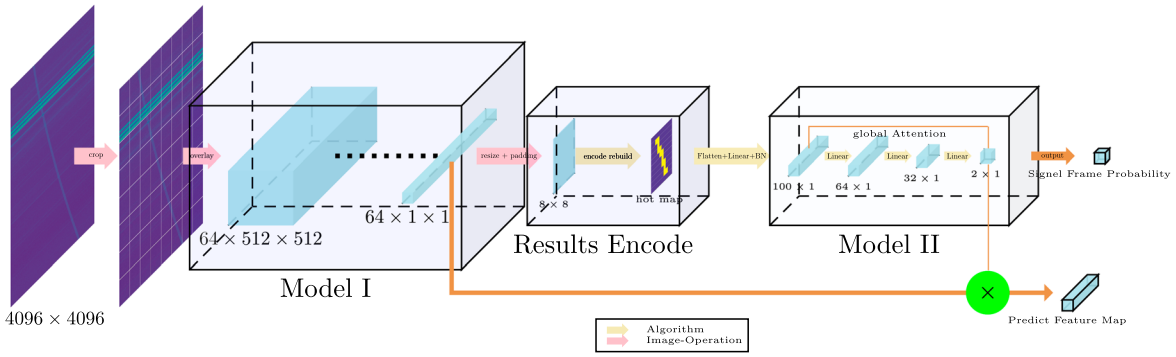

Figure 5. Architecture of TSC-Model.

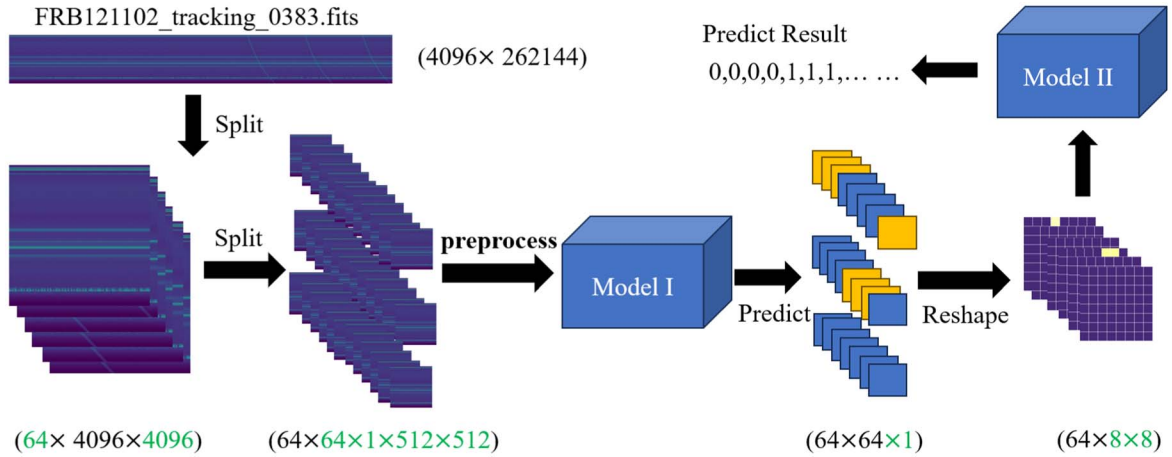

Figure 6. Process flow of TSC-Model.

4.3. TSC-Model

At the sight of the above result, we construct TSC-Model taking the EfficientNet as Model-I and GA Model as Model-II, and evaluate the performance of the TSC-Model, comparing with EfficientNet, ResNet, Inception-ResNet, DenseNet, Conv17 and FETCH model. Dataset-I and Dataset-III were used to evaluate those models. As mentioned above, Dataset-III is a data set of real FRB signals. To train the models, Dataset-I and Dataset-III were separated with the proportion of the training set at 40%, validation set at 10% and test set at 50%. While Model-I and Model-II of TSC-Model had been trained separately, TSC-Model did not require further training on Dataset-I and Dataset-III, so only the test set was used for TSC-Model.

4.3.1. Accuracy Results

We tested the accuracy of all the models on Dataset-I and Dataset-III. The result is shown in Tables 6 and 7.

The area under the curve (AUC) and receiver operating characteristic (ROC) result is shown in Figure 9.

The experimental results provide compelling evidence of the outstanding performance of the TSC model in the task of detecting FRB signals. The TSC model not only achieves the highest accuracy but also attains the second-highest recall rate, which is particularly important for FRB signal detection, as it reduces false positives while capturing more potential FRB signals. Although other models, such as EfficientNet and FETCH, demonstrate commendable precision, the TSC model exhibits a certain degree of advantage in all aspects.

The model's excellent discriminative capability is further substantiated by its AUC score of 0.996, which is nearly equivalent to the perfect value of 1. This near-optimal AUC score signifies that the model demonstrates remarkable proficiency in differentiating between positive samples (FRB signals) and negative samples (non-FRB signals). The ROC curve of the TSC model is observed to be closest to the upper left corner of the graph, indicating that it maintains outstanding

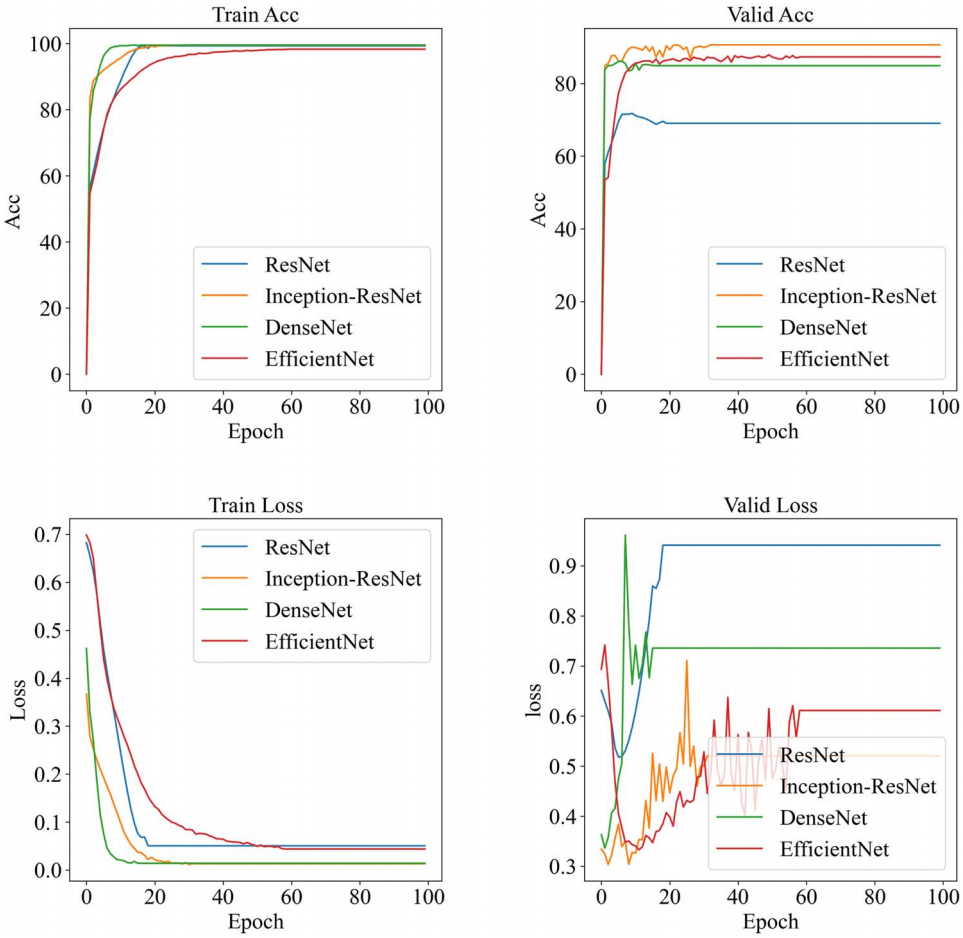

Figure 7. Training process on Dataset-II set.

Table 3
Experimental Results of the Two-stage Cascade Model, Model-I

Model Name	Accuracy	Precision	Recall	F1
ResNet	0.720	0.710	0.970	0.820
Inception-ResNet	0.915	0.980	0.890	0.932
DenseNet	0.910	0.925	0.920	0.922
EfficientNet	0.935	0.995	0.905	0.948

performance across various threshold settings. This characteristic underscores the model's excellent equilibrium between sensitivity (the capacity to detect true FRB signals) and specificity (the ability to accurately identify non-FRB signals).

These results support the superiority of the TSC model in the task of detecting FRB signals. Its performance on Dataset-I and Dataset-III reflects a commendable equilibrium among accuracy, precision, and recall. The AUC score and ROC curve convincingly demonstrate that this model is capable of delivering reliable, efficient, and sensitive FRB signal detection capabilities in practical applications.

4.3.2. Search Speed Result

To evaluate the average speed of models searching for FRB signals, we recorded the time consumed by each model to process a single FAST FITS file (4096 × 262144 pixels, 2.02 GB) on an Nvidia A100 graphics card for multiple FITS files. We then calculated the average of these times to obtain the single average search time for each model. The results are presented in Table 8. Bold indicates optimal, underline indicates sub-optimal. As can be seen, considering the accuracy achieved, the TSC-Model's average search time is quite competitive.

4.3.3. Heat Map Result

To analyze the effectiveness of the TSC-Model, we applied the Class Activation Map (CAM) (Zhou et al. 2016) to visualize the detection process of the model. From Figure 10, it can be seen that, in the CAM heat maps of samples (a) through (d), the red areas highlight the focal points of Model-I, which learns the intensity distribution. These focal points serve as the

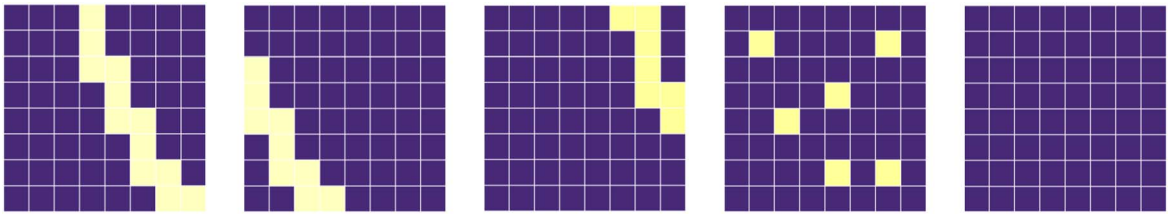

Figure 8. GA model training data samples (from left to right, positive sample, positive sample, positive sample, negative sample, negative sample).

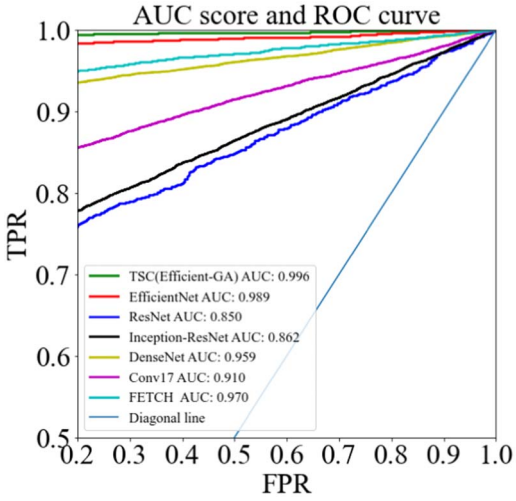

Figure 9. AUC score and ROC curve.

Table 4
Training results for Model-II

Model Name	Train Acc	Valid Acc
GA Model	99.98%	99.88%

cornerstone for the ultimate prediction outcomes, particularly for samples (b), (c), and (d). The presence of multiple red regions signifies the regions of interest identified by Model-I.

As for sample (e), the heat map noticeably indicates that the red region, shaped by noise, is starkly at odds with the dispersion pattern of the FRB. Consequently, despite Model-I flagging this region as significant, the final prediction, which also considers the dispersion structure learned by Model-II, classifies it as a negative sample.

Model-II, which learns the dispersion structure distribution, pays particular attention to the temporal relationship of multiple red regions identified by Model-I. This approach aligns perfectly with our proposed methodology, demonstrating the effectiveness of the cascaded combination of Model-I and Model-II. More experimental results can be seen at https://doi.org/10.57760/sciencedb.j00167.00010.

Table 5
Test Results for Model-II

Model Name	Accuracy	Precision	Recall	F1
GA Model	0.983	0.979	0.998	0.985

Table 6
Accuracy Performance on Dataset-I

Model Name	Accuracy	Precision	Recall	F1
TSC (EfficientNet-GA)	0.966	0.955	0.971	0.963
EfficientNet	0.928	0.993	0.898	0.943
ResNet	0.692	0.686	0.966	0.803
Inception-ResNet	0.908	0.975	0.880	0.925
DenseNet	0.897	0.919	0.912	0.915
Conv17 (Zhang et al.)	0.744	0.712	0.551	0.621
FETCH (Devansh et al.)	0.891	0.842	0.755	0.835

Table 7
Accuracy Performance on Dataset-III

Model Name	Accuracy	Precision	Recall	F1
TSC (EfficientNet-GA)	0.936	0.917	0.988	0.951
EfficientNet	0.914	0.882	0.964	0.921
ResNet	0.650	0.958	0.608	0.743
Inception-ResNet	0.818	0.699	0.919	0.794
DenseNet	0.855	0.801	0.934	0.863
conv17 (Zhang et al.)	0.699	0.688	0.966	0.803
FETCH (Devansh et al.)	0.879	0.924	0.901	0.912

5. Summary and Discussion

In reviewing the existing research on FRB signal identification, we have observed that despite the progress made, these methods still encounter significant challenges, including RFI, sensitivity to the distribution of training data, and difficulties posed by high-resolution background frames. Notably, these methods tend to overlook the intrinsic isomorphism of FRB signals, which may limit their recognition performance in complex environments.

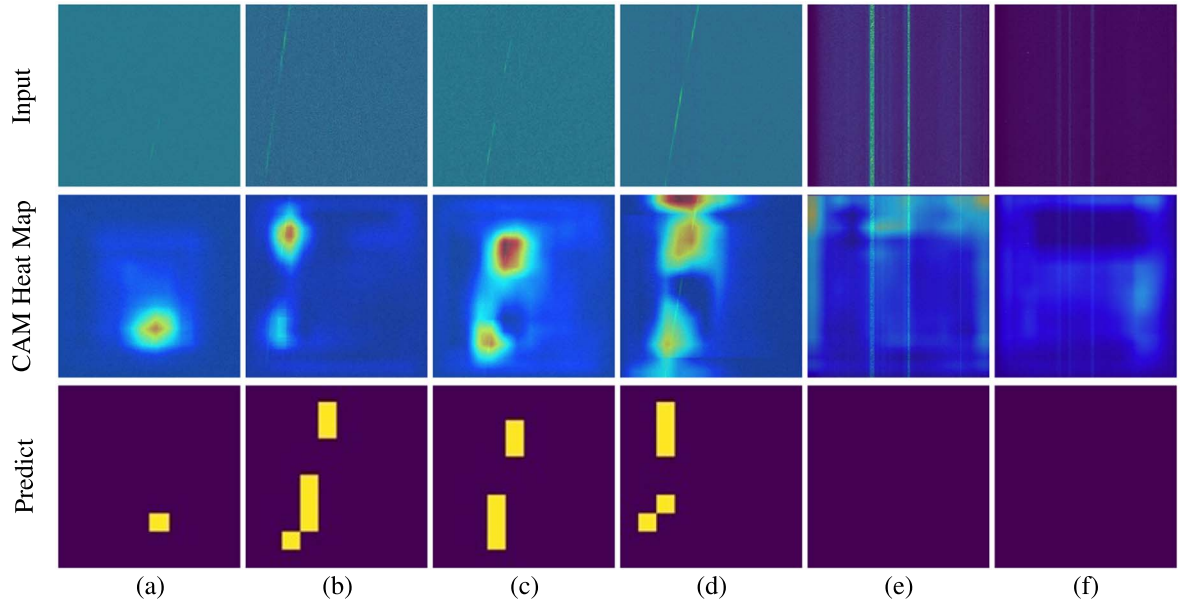

Figure 10. Heat map of detection process of TSC-Model. (From (a) to (d) are positive samples, and from (e) to (f) are negative samples).

Table 8
Average FITS File Search Time

Model Name	Times (Second)
TSC (EfficientNet-GA)	18.90
EfficientNet	23.71
ResNet	20.59
Inception-ResNet	21.71
DenseNet	21.09
Conv17 (Zhang et al.)	11.12
FETCH (Devansh et al.)	27.87

In our approach, we analyzed the FRB signal utilizing the isomorphism of the observational structure. Through rigorous experimental validation, we discovered that the two-stage cascade search method, based on the isomorphism of the observational structure, significantly enhances the predictive accuracy of the model and effectively reduces false positives caused by noise. Our method achieved an accuracy of 96.6% and an F1 score of 0.963 on the simulated data set. On the real data set, it achieved 93.6% accuracy, 98.8% recall, and an F1 score of 0.951. The main contributions in the paper are:

1. Generation of three data sets by combining simulated and real data.
2. The introduction of a two-stage cascade search method demonstrates advantages in terms of search speed, accuracy, and recall capabilities.

In the experiments conducted in this study, the specific model versions employed were Efficient-B6, ResNet101, Inception-ResNetV2, and Dense121. While the selected Efficient-B6 version may not constitute the optimal choice in certain scenarios, it remains compatible with the methodology proposed herein. Through ablation studies, the flexibility and robustness of the two-stage model architecture have been rigorously demonstrated. Upon evaluating the trade-off between temporal efficiency and accuracy, we advocate for the selection of models that exhibit both robustness and reduced time complexity for Model-I. Furthermore, for Model-II, we recommend selecting models that are sensitive to temporal relationships.

Acknowledgments

The authors wish to thank the National Astronomical Observatories, Chinese Academy of Sciences for providing the FAST drift survey data, and Dr. Pei Wang and Dr. Mao Yuan for their guidance of using the data and the astronomical background knowledge.

References

Abujar, S., Masum, A. K. M., Bhattacharya, A., Dutta, S., & Hossain, S. A. 2021, English to Bengali Neural Machine Translation Using Global Attention Mechanism in Emerging Technologies in Data Mining and Inf. Sec.. Lecture Notes in Networks and Syst., 21, ed. J. M. R. S. Tavares et al. (Singapore: Springer), 359
Bailes, M., Jameson, A., Flynn, C., et al. 2017, PASA, 34, e045
Connor, L., & Van Leeuwen, J. 2018, AJ, 156, 256

Devansh, A., Kshitij, A., Sarah, B. S., Lorimer, D. R., & Nathaniel, G. D. 2020, MNRAS, 497, 1661
Dewdney, P. E., Hall, P. J., Schilizzi, R. T., & Lazio, T. J. L. 2009, IEEEP, 97, 1482
Farah, W., Flynn, C., Bailes, M., Jameson, A., & Wolf, C. 2019, MNRAS, 488, 2989
Farah, W., Flynn, C., Bailes, M., et al. 2018, MNRAS, 478, 1209
Foster, G., Karastergiou, A., Golpayegani, G., Surnis, M., & Williams, C. J. 2017, MNRAS, 474, 3847
Gupta, V., Flynn, C., Farah, W., et al. 2021, MNRAS, 501, 2316
Hobbs, G., Miller, D., Manchester, R., et al. 2011, PASA, 28, 202
Huang, G., Liu, Z., van der Maaten, L., & Weinberger, K. Q. 2017, in Proc. of the IEEE Conf. on Computer Vision and Pattern Recognition (CVPR) arXiv:1608.06993
Kingma, D., & Ba, J. 2014, Computer Science, arXiv:1412.6980
Li, D., Wang, P., Qian, L., et al. 2018, IMMag, 19, 112
Li, D., Wang, P., Zhu, W., et al. 2021, Natur, 598, 267
Liu, Y. L., Li, J., Liu, Z. Y., et al. 2022, RAA, 22, 105007
Lorimer, D. R., Bailes, M., McLaughlin, M. A., Narkevic, D. J., & Crawford, F. 2007, Sci, 318, 777
Madison, D. R., Agarwal, D., Aggarwal, K., et al. 2019, ApJ, 887, 252
Michilli, D., Hessels, J. W. T., Lyon, R. J., et al. 2018, MNRAS, 3, 3457
Morello, V., Rajwade, K. M., & Stappers, B. W. 2021, MNRAS, 510, 1393
Niu, C.-H., Li, D., Luo, R., et al. 2021, ApJL, 909, L8
Prestage, R. M., Constantikes, K. T., Hunter, T. R., et al. 2009, IEEEP, 97, 1382
Szegedy, C., Ioffe, S., Vanhoucke, V., & Alemi, A. 2017, in Inception-v4, Inception-ResNet and the Impact of Residual Connections on Learning in Proc. AAAI Conf. Artificial Intelligence, 31, 4278
Tan, M., & Le, Q. 2019, ICML, 6105, arXiv:1905.11946
Thompson, D. R., Wagstaff, K. L., Brisken, W. F., et al. 2011, ApJ, 735, 395
Wu, J., Wen, F., & Shi, J. 2021, Direction Finding in Bistatic MIMO Radar With Direction-Dependent Mutual Coupling, IEEE Communications Letters, 25, 2231
Wagstaff, K. L., Tang, B., Thompson, D. R., et al. 2016, PASP, 128, 084503
Yatawatta, S., De Clercq, L., Spreeuw, H., & Diblen, F. 2019, IEEE, arXiv:1904.05619
Zhang, C., Wang, C., Hobbs, G., Russel, C. J., & Ren, Z. Y. 2020, A&A, 642, A26
Zhang, Y. G., Gajjar, V., Foster, G., et al. 2018, ApJ, 866, 149
Zhou, B., Khosla, A., Lapedriza, A., Oliva, A., & Torralba, A. 2016, in Proc. of the IEEE Conf. on Computer Vision And Pattern Recognition, ed. D.E. Losada & J.M. Fernández-Luna (Piscataway, NJ: IEEE), 2921